Pergamon

Cement and Concrete Research 30 (2000) 585–592

CEMENT AND CONCRETE RESEARCH

# Impedance spectra of fiber-reinforced cement-based composites A modeling approach

J.M. Torrents[a,1], T.O. Mason[a,*], E.J. Garboczi[b]

[a]Northwestern University, Center for Advanced Cement-Based Materials, Department of Materials Science and Engineering, 2225 N. Campus Drive, Evanston, IL 60208, USA

[b]National Institute of Standards and Technology, Building Materials Division, Gaithersburg, MD 20899, USA

Received 23 June 1999; accepted 7 January 2000

**Abstract**

The impedance response of conductive fiber-reinforced cement-based materials was investigated using model systems (physical simulations) consisting of conducting needles in aqueous solutions. Two discrete bulk arcs are observed in the Nyquist plots for fiber-reinforced samples, while only a single bulk arc was observed for samples without fibers. This difference is attributable to thin, resistive, and highly capacitive layers (e.g., oxide film or polarization/double layers) which reside on the surfaces of the conducting fibers. These layers fully insulate the fibers at low frequencies (near DC), so that the highly conducting fibers behave as if they were insulating fibers. At intermediate frequencies, these layers short out, so that the fibers act as highly conducting elements in the microstructure. Spreading resistance effects from the ends of the fibers play an important role in the high frequency behavior. Pixel-based computer modeling results are presented to rationalize both DC and high frequency behavior. Experimental and modeling results are used to develop an equivalent circuit model containing a frequency-switchable fiber coating element. 

*Keywords:* Electrical properties; Portland cement; Composite; Fiber reinforcement; Impedance

## 1. Introduction

Particulate and fiber reinforcements are being increasingly employed in cement-based materials to improve mechanical properties. Recently, it has been suggested that conductive fiber-reinforced concrete (c-FRC) could act as its own sensor by using the conductivity of c-FRC for stress-strain monitoring [1]. Furthermore, damage associated with permanent deformation may be detectable via deformation-induced electrical changes [2–6]. Both the DC and AC (impedance) properties of c-FRC have received attention in recent years [1–10]. To the authors' knowledge, however, a comprehensive microstructural/mechanistic model has yet to be established for the electrical properties of c-FRC, especially the frequency-dependent AC behavior.

Since the middle of the 1980s, impedance spectroscopy (IS) has been employed to investigate transport–microstructure relationships in cement-based materials [11–16] without fibers. Results have been presented in Nyquist plots, where the $y$-axis is $-\mathrm{Im}\,Z$, the $x$-axis is $\mathrm{Re}\,Z$, and $Z$ is the impedance. The Nyquist plot is parameterized by frequency, which decreases from left (high frequency) to right (low frequency). There are typically two obvious features or arcs in the impedance spectra of ordinary Portland cement paste (OPC) measured with steel electrodes. The "neat paste" curve in Fig. 1 shows a typical example. The first arc on the left, at high frequency, is that of the bulk cement paste. The second arc, found at lower frequencies on the right of Fig. 1, is associated with polarization/double layers plus any oxide film (passivation) on the electrode surfaces. This arc is usually much larger than the bulk arc, but only a small portion of the electrode arc is typically observed, as can be seen in Fig. 1. Sub-mHz measurements are required to resolve a reasonable portion of this feature, which were not made in Fig. 1. When observed at all in the present work, the electrode feature is apparent only as an upturn at the lowest frequencies (right side) of experimental Nyquist

* Corresponding author. Tel.: +1-847-491-3198; fax: +1-847-491-7820.

*E-mail address*: t-mason@nwu.edu (T.O. Mason).

[1] Permanent address: Universitat Politècnica de Catalunya, Department of Electronic Engineering (ETSETB), Jordi Girona, 1-3, 08034 Barcelona, Spain.

0008-8846/00/$ – see front matter 
PII: S0008-8846(00)00211-8

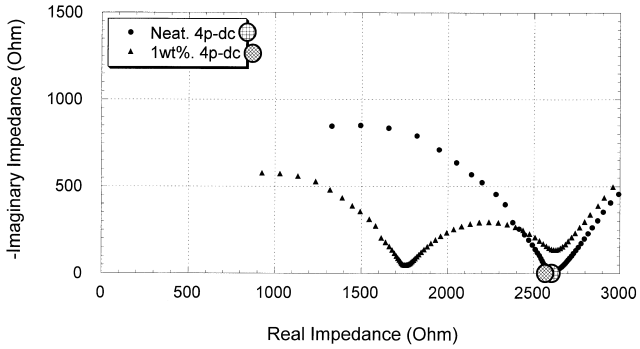


Fig. 1. Experimental Nyquist plots for 28-day old 0.4 w/c cement paste with and without 1 wt.% of steel fibers.

plots. For the sake of simplicity, a third feature, occasionally observed at intermediate frequencies in OPC/steel specimens [10], will be ignored.

When conducting fibers are added to neat cement paste, the single bulk arc is sub-divided into two arcs, as can be seen in the 1 wt.% of fibers' curve in Fig. 1. The origin of this feature must come from some combination of individual fiber geometry, fiber properties, and fiber arrangement and orientation in the cement paste matrix. The present work was undertaken to understand this effect and to understand better the electrical property–microstructure relationships in conductive fiber-reinforced cement-based materials. In this paper, experiments described were carried out on model systems consisting of physical simulations consisting of conducting needles in aqueous solutions. This was done to elucidate the principal elements of the behavior of c-FRC, without the complications of the random fiber dispersion in real c-FRC materials. In essence, the focus was on individual fiber geometry and properties, rather on the random arrangement of the fibers. The results of these experiments compared well with actual impedance spectra of conductive fiber-reinforced cement pastes, and were explained using pixel-based computer simulations, which help in establishing a model equivalent circuit for the frequency-dependent electrical properties of conductive fiber-reinforced cement-based materials.

## 2. Experimental procedure

To produce the data shown in Fig. 1, samples were prepared from Type I Portland cement at a water-to-cement (w/c) ratio of 0.4 by mass. Steel fibers (average length 2 mm, diameter of 30 μm, 1 wt.%) were dry mixed with the cement for 1 min in a Hobart planetary mixer. The water was then added, and mixing continued for 3 min at low speed, followed by 1 min of hand mixing to ensure homogenization, and three more minutes of machine mixing. Specimens were cast in rectangular polycarbonate containers (25 × 25 × 100 mm) with C-1018 plain carbon steel electrodes cast in place with a separation of 90 mm. These samples were used to establish the basic frequency-dependent behavior of c-FRC, which was then further investigated using model systems, which is the main emphasis of this paper. To confirm the true bulk resistance of the c-FRC specimens, 4-point DC measurements were also conducted. By correcting for the differing geometries in 2-point AC vs. 4-point DC measurements, the two results could be compared.

The model systems, or physical simulations, were carried out using polycarbonate containers of the identical size and shape as those used for the c-FRC samples, but employing tap water as the electrolyte. The conductivity of tap water was appropriate to simulate the conductivity of mature cement-based specimens. "Needles" of 304 steel or copper wire (0.5 mm diameter; 25, 50, 75 mm long) were positioned along the axis of the specimen container equidistant from the electrodes, suspended on insulating supports. Impedance measurements with and without the support structures (in the absence of needles) showed that these did not contribute to the spectra obtained.

Impedance measurements were carried out using a personal computer-controlled frequency response analyzer (Solartron 1260 with Z60 control software, Schlumberger, Cambridge, UK)[2] over the frequency range of 0.1 Hz to 10 MHz (10 points per decade). The excitation amplitude was varied from 25 mV to 1.0 V, with no obvious change in bulk spectral features. Spectra were analyzed with the aid of the software called "Equivalent Circuit" [17].

A FORTRAN 77 finite-difference numerical program, called *ac3d.f*, was used to carry out the pixel-based computer simulations. This program can be found at http://ciks.cbt.nist.gov/garboczi/, Chap. 2, along with a manual in HTML or hard copy format [18]. This program was designed to compute the finite frequency properties of random materials, whose microstructure can be represented by a 3-D digital image. However, the program can also be effectively used for non-random, but analytically intractable, geometries, as in the present case.

Pixels in a 3-D digital image were used to construct a representation of the experimental set-up. The length scale used was 0.5 mm/pixel, so that the model was approximately 50 × 50 × 180 pixels in size, matching the 25 × 25 × 90 mm sample (electrode–electrode) dimensions. The needles were one pixel or 0.5 mm in width, and were suspended in the middle of the sample chamber as in the experimental arrangement.

In the computation process, there was a finite difference node in the middle of each pixel. As part of the computation, bonds were assigned between each pair of nodes, reflecting the conductivities of the materials in each pair

[2] Certain commercial equipment is identified in this paper in order to adequately specify the experimental procedure. In no case does such identification imply recommendation or endorsement by the National Institute of Standards and Technology, nor does it imply that the equipment used is necessarily the best available for the purpose.

of nodes. The electrodes were taken to be highly conductive, as was the needle. No polarization layer was taken to be on the electrodes, so that the electrode arc was not included or computed. A polarization layer was taken on the surfaces of the needles. It is well known that high electrode resistances and capacitances arise due to charge transfer polarization/double layer formation and/or oxide film formation, e.g., the well-known passive oxide film which forms on steel in high pH solutions [10]. It was assumed that similar "coating" elements form on needles/fibers, as they are also metallic and embedded in an ionic conductor. The admittance of this layer on the needles was taken to be that of the electrodes (fitted from the experimental electrode arc), but adjusted for the differences in size and shape between the needle surface and the parallel plate electrodes. In this way, only the resistance and the conductance of the layer were specified, so that the unknown conductivity, dielectric constant, and thickness of the layer did not need to be individually determined. The water pixels had the correct admittance for the tap water used ( $\sim 0.03$ S/m). The needle itself had a bulk DC conductivity approximately $10^9$ times that of the tap water.

Once the model geometry and admittances were set up, a uniform electric field was applied along the needle direction, as was done experimentally, and a conjugate gradient method was used to find the solution to the complex conductivity problem. The frequency was systematically varied, similar to experiment, and the Nyquist plot determined.

## 3. Results and discussion

Fig. 1 displays the impedance spectra in a Nyquist plot for a neat w/c = 0.4 paste specimen and a typical c-FRC composite specimen, both at 28 days of hydration. The beginning of the large electrode arc is visible at the right in each spectrum. The intersection of this arc with the bulk arc(s) in Fig. 1 represents the true bulk resistance, as was confirmed by 4-point DC measurements. This point is denoted throughout this paper as $R_{DC}$. Whereas one bulk arc is evident in the case of the neat paste, two arcs are apparent in the c-FRC spectrum. In other words, the presence of 1 wt.% chopped steel fibers had little or no effect on the value of $R_{DC}$, but the AC behavior was dramatically changed, so that the single bulk arc became divided into two separate arcs.

This behavior was successfully duplicated by the physical simulations of needles in tap water. These physical simulations neglect the random fiber arrangement and orientation, and focus only on the effects of fiber properties in the cement paste matrix and individual fiber geometry. As will be shown below, by neglecting the random fiber arrangement and orientation, the main features of the two-arc behavior were still captured, even though there will of course be some quantitative differences with experiments at high fiber loadings. Therefore, the principal features of the two bulk arc behavior are mainly only a function of individual fiber geometry and properties, and not of the random fiber arrangement and orientation.

Fig. 2 shows Nyquist plots for the tap water alone (before and after adding needles) and with 304 stainless steel needles 25, 50, or 75 mm long. It can be seen that the single bulk arc in the no-needle (tap water only) case is subdivided into two arcs of varying size by the presence of the conductive needle. Furthermore, the value of $R_{DC}$, the bulk resistance, at the intersection of the real axis with the electrode arc on the extreme right, does not change significantly with the addition of the needles. However, the value of the real resistance at the intersection between the two bulk arcs, denoted $R_{int}$, does decrease as the length of the fibers increases. The longer fibers of course have a somewhat larger volume concentration. Since the value of $R_{DC}$ is fairly constant, and $R_{int}$ decreases as the fiber length increases, the size of the right-hand bulk arc increases, and the size of the left-hand bulk arc decreases, as the fiber length increases.

Additional physical simulations were conducted wherein an increasing number of parallel 50 mm long needles (in this case copper, 0.5 mm diameter) were suspended in tap water on an insulating mesh support framework. The minimum needle-to-needle separation was 5 mm. In Fig. 3, as the number of needles increases from 1 to 16, the left-hand bulk arc shrinks, the right-hand bulk arc grows, and the intersection between the two arcs, $R_{int}$, decreases. This decrease can be understood simply.

In Fig. 4, the real bulk resistance at the intersection of the two bulk arcs, $R_{int}$, normalized by the DC bulk resistance, $R_{DC}$, is taken from the data in Figs. 2 and 3 and plotted vs. the total length of the two tap water regions, $L$, lying between the ends of the needles and the electrodes, where $L$ is the difference between the total sample length between the electrodes, 90 mm, and the needle length. Also plotted (lower dashed line) is the resistance of just this tap water region, $R = \rho L/A$, where $\rho$ is the tap water resistivity and $A$ is the cross-sectional area of the sample, normalized by the

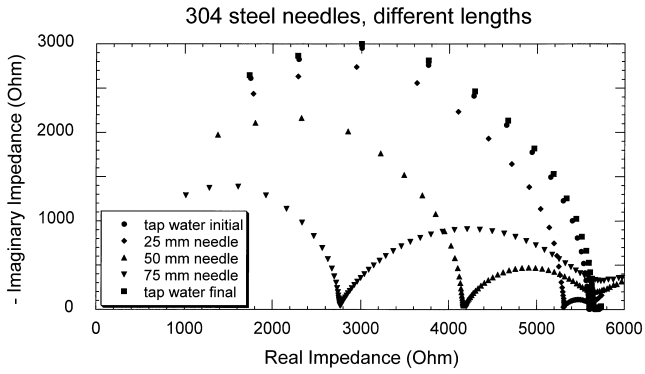


Fig. 2. Experimental Nyquist plots for a single 0.5 mm diameter needle suspended in tap water, for three different needle lengths (25, 50, and 75 mm), and for the plain tap water both before and after adding the needles.

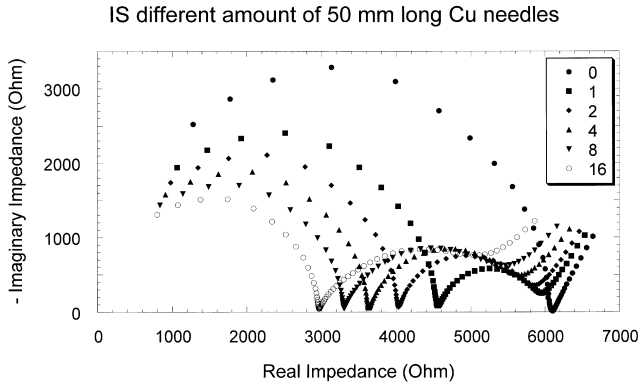


Fig. 3. Experimental Nyquist plots for various numbers of 0.5 mm diameter, 50 mm long needles suspended in tap water, along with the plain tap water.

value at $L = 90$ mm. The upper solid line without data points is the computer simulation result (described in detail later) for single needles of various lengths. The solid curve with three data points is the single needle experimental result from Fig. 2. The multiple-needle experimental data from Fig. 3 are all plotted at $L = 40$ mm, since in this case, the needles were all 50 mm long. If the 50 mm needle region was a solid highly conducting region, the resistance at the intersection, $R_{int}$, would be composed of only the resistance of the two 20 mm tap water regions at either end of the fiber array that lie between the needles and the electrodes. As more needles are added, the needle region approaches this limit, and the multiple-needle data points approach the $R$ vs. $L$ line as the number of needles increases.

The exact way in which these data points approach the $R$ vs. $L$ line is of interest. One might think that resistance of the needle region would decrease simply inversely with the cross-sectional area of the needles, as more and more of this region becomes occupied by highly conducting material. However, the resistance of the needle region decreases much faster than the needle cross-sectional area, because current is concentrated into the needles. The needles have a much *greater* lowering effect on the resistance than just their cross-sectional area would imply. However, the needles do not lower the resistance as much as if the entire needle region were highly conducting, as only part of the needle region is made up of highly conducting material.

The effect of the needles at the $R_{int}$ point can then be thought of in two ways, either by comparing their effect to the matrix of tap water without needles, or by comparing their effect to having the needle region totally filled with highly conducting material. The first point of view is discussed more fully in the Appendix. The second point of view is often used in the IS literature, and is associated with a concept called the *spreading resistance*. This concept will be used in the rest of this discussion.

To understand the idea of spreading resistance, consider a unit cube of conducting material with electrodes covering opposite faces. When current is applied, the resistance is just that of the entire block, where current is uniform within the block. Now suppose one electrode were to be replaced by a wire whose tip just touched the cube face. The measured resistance is now much greater, since all the current, which begins fairly uniformly at the flat electrode face, has to bunch together at the wire tip in order to pass out of the material. The difference between the two measured resistances is called the spreading resistance. Therefore, in Fig. 4, the differences between the upper curves and data points, compared to the lower dashed curve, are just the various spreading resistances, which are different for different needle geometries. The spreading resistance is due to current-bunching in the vicinity of the wire tip and inhomogeneous current density in the bulk. These concepts are developed further below.

Using pixel-based computer simulations, the mechanisms of the two-bulk arc behavior were tested and elucidated. The impedance diagrams of Figs. 2 and 3 were successfully simulated using the pixel network and the thin layer on the needles, as described above. The computer

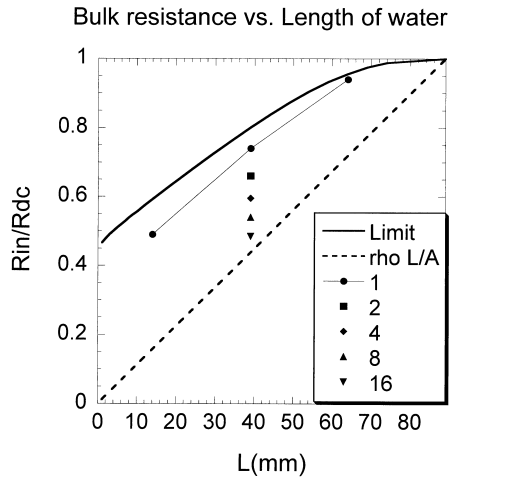


Fig. 4. The ratio $R_{int}/R_{DC}$ for various geometries, vs. the length of the needle-free section of the sample, from experiment and computer simulation.

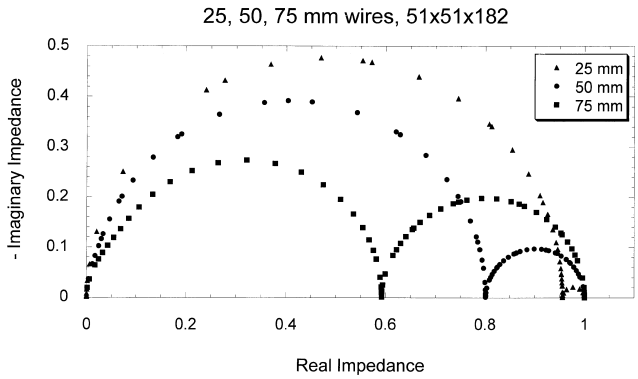


Fig. 5. Computer-simulated Nyquist plots, in units where $R_{DC}$ for the plain tap water-filled cell is unity, for a single 0.5 mm diameter needle suspended in tap water, for three different needle lengths (25, 50, and 75 mm).

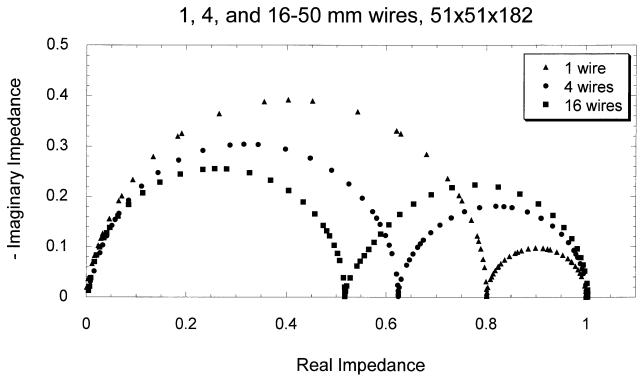


Fig. 6. Computer-simulated Nyquist plots for various numbers of 0.5 mm diameter, 50 mm long needles suspended in tap water, in units where $R_{DC}$ for the plain tap water-filled cell is unity.

simulation results are shown in Figs. 5 and 6, which correspond to Figs. 2 and 3, respectively. The resulting agreement with the experimental Nyquist plots was quite good. Furthermore, the simulated ratio of $R_{int}$ to $R_{DC}$ , in both the single and multiple needle cases, agreed well with the experimental values.

Fig. 5 shows the computer simulation results for single needles of different lengths. The qualitative aspects of the experimental and computer simulation plots can now be readily explained, bearing in mind that the volume fraction of the single needles is very small, certainly less than 1%. It has been shown [19,20] that long, thin needle-like inclusions produce little effect on the bulk conductivity when they are insulating compared to the matrix, but have great effect when they are highly conducting compared to the matrix. Once the aspect ratio gets beyond 10 or so, all needles have essentially the same effect on the conductivity when they are insulating. However, when the needles are highly conducting, then the effect of the needle on the bulk conductivity is very sensitive to the aspect ratio [20] (see Appendix).

In Fig. 5 (model) and Fig. 2 (experiment), therefore, the DC resistance at the low frequency end of the arcs on the right of the graph, $R_{DC}$, is found for the case when the needles are insulating, because the polarization layer is insulating at this frequency. Because insulating needle-like inclusions have little effect on the conductivity, the resistance at this point is essentially just that of the tap water. The needle length does not matter very much at this point [19,20]. As the frequency is increased, however, the impedance of the "coating" on the needle goes to zero and a low frequency arc (on the right) is traced out until the imaginary impedance touches the real axis. At this point, the real resistance, $R_{int}$, is that of the matrix plus a highly conducting needle. Now, the effect of the highly conducting needles is quite sensitive to the needle length. Since these needles are cylindrical wires, with the same diameter, the aspect ratio varies linearly with the length. The value of $R_{int}$ then moves left to lower resistance as the needle length increases.

In the computer simulation technique used, all local current density information is available as well as the global average current or admittance. This has been used, in the 50 mm long, single needle case, to demonstrate the current-bunching ideas and lend support to the fact that the needle acts differently at different frequencies. At frequencies corresponding to the $R_{DC}$ and $R_{int}$ points on the arc, the current magnitudes along a longitudinal slice that included the needle were saved. These currents were converted to gray scale images using a gray scale table that brought out the detail in how the current densities varied spatially. The results are shown in Fig. 7. Fig. 7(top) shows the local currents at a frequency when the needle is insulating, and

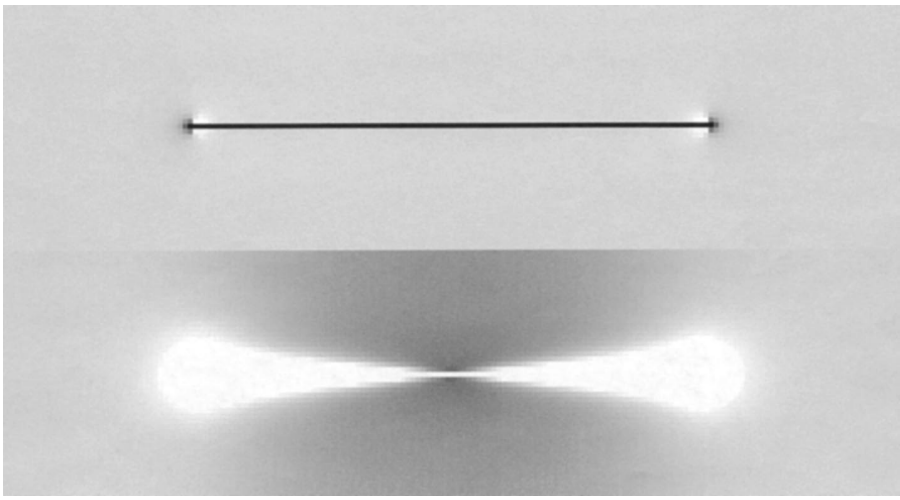

Fig. 7. Gray scale images of a longitudinal section of the computer simulation cell, in the plane of the needle, for the 50 mm needle — (top) at DC frequencies ($R_{DC}$ in Fig. 5), (bottom) at a frequency where the needle is highly conducting ($R_{int}$ on Fig. 5). White is high current density, dark gray is low current density. The gray scale was chosen so as to bring out the detail of the current distributions.

Fig. 7(bottom) shows the currents at a frequency when the needle is highly conducting. In Fig. 7(top), the current is uniform and is almost undisturbed by the presence of the needle. However, the presence of the highly conducting needle in Fig. 7(bottom) clearly alters the initially uniform current density. The needle draws current into itself, causing much higher currents near the tips and depleting current in regions surrounding the midpoint of the needle, since most of the current is now going through the needle instead of the tap water matrix.

Fig. 7(bottom) also aids in visualizing the two contributions to overall resistance at $R_{int}$, when the wire is conducting. Towards the outer ends (external electrodes), there are bulk contributions due to the tap water like the low frequency (insulating wire) situation in Fig. 7(top). These are in series with spreading resistances as current bunches to the tips of the wire. Roughly speaking, we may associate the former (bulk) contribution with the lower line in Fig. 4 and the latter (spreading resistance) contribution with the difference between the upper and lower lines in the same plot. Note that as the number of wires increases from 1 to 16 in Fig. 4, the value of $R_{int}$ approaches the lower line, i.e., the value corresponding to that of the outer tap water regions. Since the spreading resistances of adjacent wires act roughly in parallel, neglecting interaction effects, their contribution becomes less and less significant as their number increases.

A simplified equivalent circuit based upon this interpretation is presented for a single fiber in cement paste in Fig. 8. In addition to the overall bulk cement paste RC element (upper path), there is a parallel path consisting of outer paste RC elements (between the external electrodes and the spreading resistance regions) and spreading resistance RC elements. Note that the fiber/coating has been represented by a frequency-activated switch. The switch is actually an additional RC element with parameters as described above in the simulation section. Its representation as a frequency-activated switch is useful for the sake of discussion. (The actual fiber resistance is ignored since it is negligibly small.) The time constants of the bulk paste, outer paste, and spreading resistance elements are assumed to be identical. At DC and low frequency AC, the bottom path is essentially an open circuit due to the high "coating" resistance, and the circuit behaves as if the fibers (bottom path) are absent; the DC resistance/capacitance is that of the paste matrix (upper path). As frequency increases, however, the impedance of the "coating" RC element in the bottom path goes to zero and the switch is thrown. The resistance now measured is predominantly the lower path, or the sum of outer paste plus spreading resistance contributions.

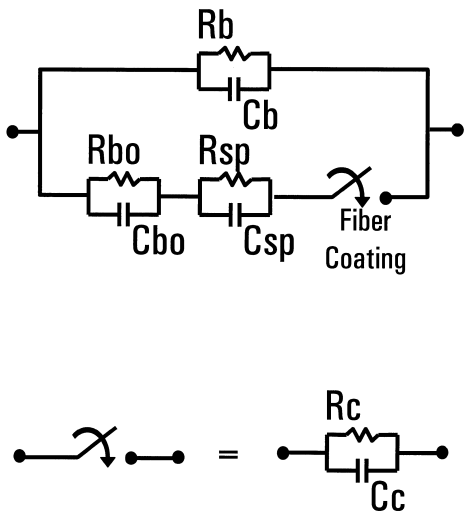


Fig. 8. Simplified equivalent circuit model for the needle/tap water system. $R_b$, $C_b$ are bulk paste parameters, $R_{bo}$ and $C_{bo}$ are outer paste parameters (between the electrodes and the spreading resistance regions when the wires are conducting), and $R_{sp}$ and $C_{sp}$ are the spreading impedance parameters.

Based upon physical and computer simulations, the frequency-switchable coating model is capable of interpreting the general features of the IS spectra of c-FRC, which are dual bulk arcs with fibers vs. single arcs without fibers. The DC resistance (low frequency bulk intercept in Nyquist plots) is largely unaffected by the presence of a low volume fraction of conductive fibers. This is due to the fact that their polarization resistances/double layer capacitances and/or oxide film coatings serve to completely insulate them under such conditions. As the frequency increases, however, the coating/polarization impedance disappears and the fibers then act as short-circuit paths in the composite. The residual resistance $R_{int}$, the diameter of the high frequency bulk arc, has contributions from fiber-to-electrode and fiber-to-fiber bulk resistance plus an important spreading resistance component. The fiber aspect ratio, which was a negligible factor in DC resistivity, now plays a major role.

These results provide the basis for an ongoing study of the impedance response of fiber-reinforced composites. Subsequent work will address the issues of fiber orientation, fiber-to-fiber distances (i.e., fiber volume fraction), fiber/matrix de-bonding, fiber pull-out, and how these factors influence the impedance spectra of cement-based composites with conductive fiber additions. The effects of deformation/damage of the fiber/matrix on the IS spectra will also be explored.

## 4. Conclusions

Conductive fibers, when added to cement-based composites, appear to have a negligible effect on the DC resistance, but play a dominant role in the intermediate and high frequency AC behavior. The present work, utilizing both physical and computer simulations, has shown that these phenomena arise due to polarization layers (charge transfer resistance/double layers and/or oxide films layers) on the surfaces of conductive fibers. Under DC and low frequency AC excitation, these layers act to insulate the fibers and their effect on transport through the composite is negligible. As frequency is increased, however, the surface layer impe-

dance goes to zero causing the fibers to act as short-circuits in the composite. The result is the subdivision of the single Nyquist arc, in the case with no fibers, into two separate arcs. Whereas the fiber aspect ratio is a negligible factor in the DC resistance and low frequency AC impedance, it plays a major role at high frequencies. The diameter of the high frequency arc is a combination of bulk paste resistance (between fibers and between fibers and electrodes) and spreading resistance due to current-bunching at the fiber tips. Equivalent circuits were presented to explain both DC and high frequency behavior based upon a frequency-switchable fiber coating model.

## Acknowledgments

This work was supported by the National Science Foundation Science and Technology Center for Advanced Cement-Based Materials under grant no. CHE-91-20002. JMT acknowledges the support of the Spanish Government through the Secretary of the State for Universities, Research and Development of the Ministry of Education and Culture under grant no. PR98-0036975531.

## Appendix

In this appendix, more mathematical detail is given to describe the phenomena measured in the single fiber experiments, and an analytical example of a coated sphere is given. The dilute limit (defined below) is considered because that is the only situation where exact closed-form analytical results are known in 3-D.

Consider a composite material in the dilute limit: a uniform matrix containing a small volume fraction of inclusions. By dilute limit, it is meant that the inclusions are far enough apart so that the effect that each has on the overall properties is independent of the other particles. Only the linear conductivity problem is considered, where the conductivity of the matrix phase is $\sigma_1$, and the conductivity of the inclusions is $\sigma_2$. These conductivities are complex. The equation to be solved, for steady-state current flow at a single frequency, is the time independent complex current continuity equation Eq. (A.1),

$$\nabla \cdot j = 0 \tag{A.1}$$

where $j(\vec{r}) = \sigma(\vec{r})\vec{E}(\vec{r})$, $\vec{E} = -\nabla V$, and the potential $V$ and the normal current are continuous at the boundaries of the inclusions, and are in general complex quantities [21]. In the dilute limit, only the fields around a single inclusion need to be solved. This has been done for many particle shapes analytically and numerically [19]. From these solutions, the frequency-dependent intrinsic conductivity, $[\sigma(\delta)]$, can be computed, where $\delta = \sigma_2/\sigma_1$ is the contrast between the phases. The fields can be isotropically averaged, to simulate a random orientation of the particle, or the intrinsic conductivity can be defined for a single orientation. The conductivity of the composite, with respect to the conductivity of the matrix, is given exactly by Eq. (A.2):

$$\sigma/\sigma_1 = 1 + [\sigma(\delta)]c \tag{A.2}$$

where $c$ is the inclusion volume fraction.

Most of the known solutions for $\sigma(\delta)$ have been for the special cases of $\delta \gg 1$, where $[\sigma(\delta)]$ is denoted as $[\sigma]_\infty$, or $\delta \ll 1$, in which $[\sigma(\delta)] = [\sigma]_o$ [19]. The intrinsic conductivity is negative when $\delta < 1$, and positive when $\delta > 1$. Generally, the intrinsic conductivity depends on the shape of the inclusion particle and the value of $\delta$. However, in the two limits mentioned, the intrinsic conductivity becomes a function of shape only.

Now consider the case of long, thin inclusions. It has been shown that $[\sigma]_\infty$ increases with the aspect ratio (length to width ratio) of the fiber, so its value can be extremely large for thin objects. For the case of equal width fibers, then the intrinsic conductivity in this limit will increase with the length of the fiber. However, the value of $[\sigma]_o$ goes to a limit of about $-5/3$ for long thin objects [19]. Therefore, in the DC limit, a small volume fraction (less than 1%) of insulating fibers will have almost no effect on the DC conductivity, while the same amount of highly conducting fibers will have a great effect on the overall conductivity. This effect was seen in the simulation results shown in Figs. 5 and 6. In the dilute limit, the diameter of the arc at low frequency (right-hand arc) in the Nyquist plot is then the difference between and $R_{DC} \approx \{\sigma_1 + [\sigma(\delta)]_o c\}^{-1}$ and $R_{int} \approx \{\sigma_1 + [\sigma(\delta)]_\infty c\}^{-1}$.

For inclusions having a uniform thickness coating of a third phase, so that solving the dilute limit means solving a three-phase problem, the only known analytical results are for spheres, so that the following analytical example is for the dilute limit of coated spherical inclusions. That is why the needle cases looked at in this paper required computer simulation, since no analytical treatment was available. The sphere example is also relevant to a cement and concrete audience [22].

For a sphere of radius $b$ and conductivity $\sigma_2$, surrounded by a layer of thickness $h$ and conductivity $\sigma_3$, in a matrix of conductivity $\sigma_1$, the intrinsic conductivity in terms of the volume fraction, $c$, of the inner particle is given by:

$$[\sigma] = \frac{3[(\sigma_2 - \sigma_3)(2\sigma_3 + \sigma_1) + \beta(\sigma_2 + 2\sigma_3)(\sigma_3 - \sigma_1)]}{[(\sigma_2 + 2\sigma_3)(\sigma_3 + 2\sigma_1) + (2/\beta)(\sigma_2 - \sigma_3)(\sigma_3 - \sigma_1)]} \tag{A.3}$$

where $\beta = [(b + h)/b]^3$ [22].

When $\sigma_3$, the layer conductivity, is zero, Eq. (A.3) reduces to $-3\beta/2$, the intrinsic conductivity for an insulating sphere of radius $b + h$ [19]. This result is independent of the value of $\sigma_2$, so that the object acts as if it were entirely made of insulating material. This is true for any thickness $h$

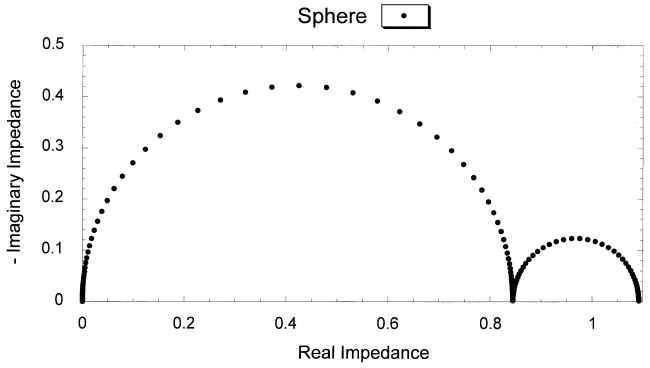


Fig. 9. The theoretical Nyquist plot of Eq. (A.3), in units where $R_{DC}$ for the matrix is unity, for a coated sphere. The coating thickness is slightly more than 5% of the radius of the sphere, and the volume fraction of dilute spheres was 5%.

(disregarding any quantum tunneling phenomena), because no current can get through the insulating outer layer.

When $\sigma_3$, the layer conductivity, is much bigger than $\sigma_1$ or $\sigma_2$, Eq. (A.3) reduces to $3\beta$, the intrinsic conductivity for a highly conducting sphere of radius $b + h$ [19]. As long as $\sigma_3$ is much bigger than $\sigma_1$ or $\sigma_2$, this result is independent of the value of $\sigma_2$, so that the object acts as if it were highly conducting, for any thickness $h$. This is because the highly conducting surface layer channels all the current around the object. When the inner object is also highly conducting, so that both $\sigma_3$ and $\sigma_2$ are large, then this limit is also reached.

For the complex case, as long as the time constant of the shell is well-separated from that of the matrix, then the layer conductivity will effectively go from insulating to highly conducting before the matrix changes very much, so the conductivity will go from $\sigma/\sigma_1 = 1 + [\sigma]_o c < 1$ to $\sigma/\sigma_1 = 1 + [\sigma]_\infty c > 1$. The resistance will of course have the opposite behavior. Fig. 9 shows the result for an spherical inclusion volume fraction of 5%. The units are such that the conductivity of the matrix is unity. Note the real axis intercepts at $R_{DC} = 1/(1-3\beta c/2)$ and $R_{int} = 1/(1+3\beta c)$, for $c = 0.05$ and $\beta = 1.16$.

## References

[1] P.-W. Chen, D.D.L. Chung, Concrete as a new strain–stress sensor Composites B 27 1 (1996) 11–23.

[2] X. Fu, D.D.L. Chung, Contact electrical resistivity between cement and carbon fiber: Its decrease with increasing bond strength and its increase during fiber pull-out Cem Concr Res 25 7 (1995) 1391–1396.

[3] X. Fu, D.D.L. Chung, Self-monitoring of fatigue damage in carbon fiber reinforced cement Cem Concr Res 26 1 (1996) 15–20.

[4] X. Fu, E. Ma, D.D.L. Chung, W.A. Anderson, Self-monitoring in carbon fiber reinforced mortar by reactance measurement Cem Concr Res 27 6 (1997) 845–852.

[5] D.D.L. Chung, Self-monitoring structural materials Mater Sci Eng R22 (1998) 57–78.

[6] X. Wang, X. Fu, D.D.L. Chung, Electromechanical study of carbon fiber composites J Mater Res 13 11 (1998) 3081–3092.

[7] N. Banthia, S. Djeridane, M. Pigeon, Electrical resistivity of carbon and steel micro-fiber reinforced cements Cem Concr Res 22 (1992) 804–814.

[8] P. Gu, Z.Z. Xu, P. Xie, J.J. Beaudoin, An A.C. impedance spectroscopy study of micro-cracking in cement-based composites during compressive loading Cem Concr Res 23 (1993) 675–682.

[9] P. Xie, P. Gu, J.J. Beaudoin, Electrical percolation phenomena in cement composites containing conductive fibres J Mater Sci 31 (1996) 4093–4097.

[10] S.J. Ford, J.D. Shane, T.O. Mason, Assignment of features in impedance spectra of the cement-paste/steel system Cem Concr Res 28 12 (1998) 1737–1751.

[11] W.J. McCarter, S. Garvin, H. Bouzid, Impedance measurements on cement paste J Mater Sci Lett 7 (1988) 1056–1057.

[12] C.A. Scuderi, T.O. Mason, H.M. Jennings, Impedance spectra of hydrating cement pastes J Mater Sci 26 (1991) 349–353.

[13] P. Gu, Z. Xu, P. Xie, J.J. Beaudoin, Application of A.C. impedance techniques in studies of porous cementitious materials I Cem Concr Res 23 (1993) 531–540.

[14] P. Gu, Z. Xu, P. Xie, J.J. Beaudoin, Application of A.C. impedance techniques in studies of porous cementitious materials II Cem Concr Res 23 (1993) 853–862.

[15] P. Gu, Z. Xu, P. Xie, J.J. Beaudoin, Application of A.C. impedance techniques in studies of porous cementitious materials III Cem Concr Res 23 (1993) 1007–1015.

[16] B.J. Christensen, R.T. Coverdale, R.A. Olson, S.J. Ford, E.J. Jennings, T.O. Mason, Impedance spectroscopy of hydrating cement-based materials: Measurement, interpretation, and application J Am Ceram Soc 77 11 (1994) 2789–2804.

[17] B.A. Boukamp, Equivalent Circuit (EQUIVCRT.PAS), University of Twente, Dept. of Chemical Engineering, The Netherlands, 1990.

[18] E.J. Garboczi, Finite element and finite difference programs for computing the linear electric and elastic properties of digital images of random materials, NIST Internal Report 6269, 1998. Also available at http://ciks.cbt.nist.gov/garboczi/, Chap. 2.

[19] J.F. Douglas, E.J. Garboczi, Intrinsic viscosity and the polarizability of particles having a wide range of shapes Adv Chem Phys 91 (1995) 85–153.

[20] E.J. Garboczi, J.F. Douglas, Intrinsic conductivity of objects having arbitrary shape and conductivity Phys Rev E 53 6 (1996) 6169–6180.

[21] Z. Hashin, Analysis of composite materials—a survey J Appl Mech 50 (1983) 481–505.

[22] E.J. Garboczi, L.M. Schwartz, D.P. Bentz, Modeling the influence of the interfacial zone on the DC electrical conductivity of mortar Adv Cem Based Mater 2 5 (1995) 169–181.